Jahn-Teller Switching of a Redox-active Nickel(III) Center in a Homoleptic Thiolato Metalloligand Environment

Masahiro Kouno,[a,b] Naoto Kuwamura,[a,c] Nobuto Yoshinari,[a*] Tatsuhiro Kojima,[a] Malcolm A. Halcrow,[d] Kohei Yamagami,[e,f] Akira Sekiyama,[g] and Takumi Konno[a,h*]*

[a] Department of Chemistry, Graduate School of Science, Osaka University, Toyonaka, Osaka 560-0043, Japan

[b] Hyogo Prefectural Institute of Technology, Kobe, Hyogo 654-0037, Japan

[c] Center for Promotion of Higher Education, Kogakuin University, Hachioji, Tokyo 192-0015, Japan

[d] School of Chemistry, University of Leeds, Woodhouse Lane, Leeds LS2 9JT, U.K.

[e] Japan Synchrotron Radiation Research Institute (JASRI), Sayo-gun, Hyogo 679-5198, Japan

[f] Institute for Solid State Physics, The University of Tokyo, Kashiwa, Chiba 277-8581, Japan

[g] Division of Materials Physics, Graduate School of Engineering Science, Osaka University, Toyonaka, Osaka 560-8531, Japan

[h] Department of Chemistry, Faculty of Science, National Taiwan Normal University, Taipei 11677, Taiwan

ABSTRACT: Treatment of nickel(II) nitrate with the iridium(III) metalloligand *fac*-[Ir(apt)$_3$] (apt = 3-aminopropanethiolate) gave the trinuclear complex [Ni{Ir(apt)$_3$}$_2$](NO$_3$)$_3$ ([**1**$_{\mathbf{Ir}}$](NO$_3$)$_3$), in which the nickel center has a formal oxidation state of +III. Chemical or electrochemical oxidation and reduction of [**1**$_{\mathbf{Ir}}$](NO$_3$)$_3$ generated the corresponding trinuclear complexes [Ni{Ir(apt)$_3$}$_2$](NO$_3$)$_4$ ([**1**$_{\mathbf{Ir}}$](NO$_3$)$_4$) and [Ni{Ir(apt)$_3$}$_2$](NO$_3$)$_2$ ([**1**$_{\mathbf{Ir}}$](NO$_3$)$_2$) with one-electron oxidated and reduced states, respectively. Single-crystal X-ray crystallography revealed that the nickel center in [**1**$_{\mathbf{Ir}}$](NO$_3$)$_3$ is situated in a highly distorted octahedron due to Jahn-Teller effect, while the nickel center in each of [**1**$_{\mathbf{Ir}}$](NO$_3$)$_4$ and [**1**$_{\mathbf{Ir}}$](NO$_3$)$_2$ adopts a normal octahedral geometry. Crystals of [**1**$_{\mathbf{Ir}}$](NO$_3$)$_3$·2H$_2$O are dehydrated on heating, while retaining their single-crystallinity. The dehydration induces temperature-dependent dynamic disorder of the Jahn-Teller distortion at the nickel(III) center, which is largely quenched upon rehydration of the crystal.

Introduction

Coordination compounds with a high valent nickel(III) center have long received considerable attention because nickel(III) species are important intermediates in biological and artificial catalytic cycles.[1-9] To date, a number of nickel(III) coordination compounds have been synthesized using a variety of ligands with carbene C-donor,[10] imine/amine N-donor,[11] alkoxide O-donor,[12] or thiolate/thioether S-donors.[13-17] The latter have been of particular interest, as structural and functional models for technologically important NiFe hydrogenases, and other nickel enzymes.[18] However, studies on this class of compounds have mainly focused on their catalytic activities. The fundamental nature of nickel(III) species, such as their spectroscopic and redox properties, are still less investigated due to their instability under ambient conditions.[19] In addition, examples of

structurally characterized octahedral nickel(III) species with a low-spin d^7 electronic configuration, which are expected to show a Jahn-Teller distortion, are relatively rare.[14,20-22] In these circumstances, it is valuable to create a new coordination system, which allows us the systematic investigation of redox characteristics and Jahn-Teller distortion behavior of an octahedral nickel(III) center.

In the course of our long-standing program of using thiolato metal complexes as S-donating metalloligands in multinuclear cluster assemblies,[23,24] we recently reported the S-bridged trinuclear complex, $[Ni\{Rh(apt)_3\}_2]^{3+}$ ($[\mathbf{1_{Rh}}]^{3+}$; apt = 3-aminopropanethiolate),[25] where *fac*-$[Rh(apt)_3]$ acts as a tripodal S-donating metalloligand to nickel.[26-29] In $[\mathbf{1_{Rh}}]^{3+}$, the nickel center adopts a Jahn-Teller distorted octahedral geometry with a +III oxidation state, which is reversibly oxidized and reduced to form nickel centers with +IV and +II oxidation states, respectively. Notably, all the three species are stable enough to be isolated as single crystals, whose structures were established by X-ray analysis.

Motivated by these intriguing results, we have now synthesized the metalloligand *fac*-$[Ir(apt)_3]$ and used it to create trinuclear $[Ni\{Ir(apt)_3\}_2]^{3+}$ ($[\mathbf{1_{Ir}}]^{3+}$), which is analogous to $[\mathbf{1_{Rh}}]^{3+}$. We found that $[\mathbf{1_{Ir}}]^{3+}$ is reversibly converted to $[Ni\{Ir(apt)_3\}_2]^{2+}$ ($[\mathbf{1_{Ir}}]^{2+}$) and $[Ni\{Ir(apt)_3\}_2]^{4+}$ ($[\mathbf{1_{Ir}}]^{4+}$) by reduction and oxidation reactions, as in the case of $[\mathbf{1_{Rh}}]^{3+}$ (Scheme 1). However, the $[\mathbf{1_{Ir}}]^{3+/2+}$ and $[\mathbf{1_{Ir}}]^{3+/4+}$ redox potentials are appreciably more negative than those of $[\mathbf{1_{Rh}}]^{3+/2+}$ and $[\mathbf{1_{Rh}}]^{3+/4+}$. In addition to the isolation and structural characterization of all the nitrate salts of $[\mathbf{1_{Ir}}]^{2+}$, $[\mathbf{1_{Ir}}]^{3+}$, and $[\mathbf{1_{Ir}}]^{4+}$, we found that a Jahn-Teller distortion of the Ni^{III} center in $[\mathbf{1_{Ir}}]^{3+}$ is reversibly activated to dynamic disorder by a single-crystal-to-single-crystal dehydration/rehydration process. While it is a well-known phenomenon in copper(II) chemistry,[30,31] this is a rare observation of Jahn-Teller disorder in a nickel(III) complex.[14,20]

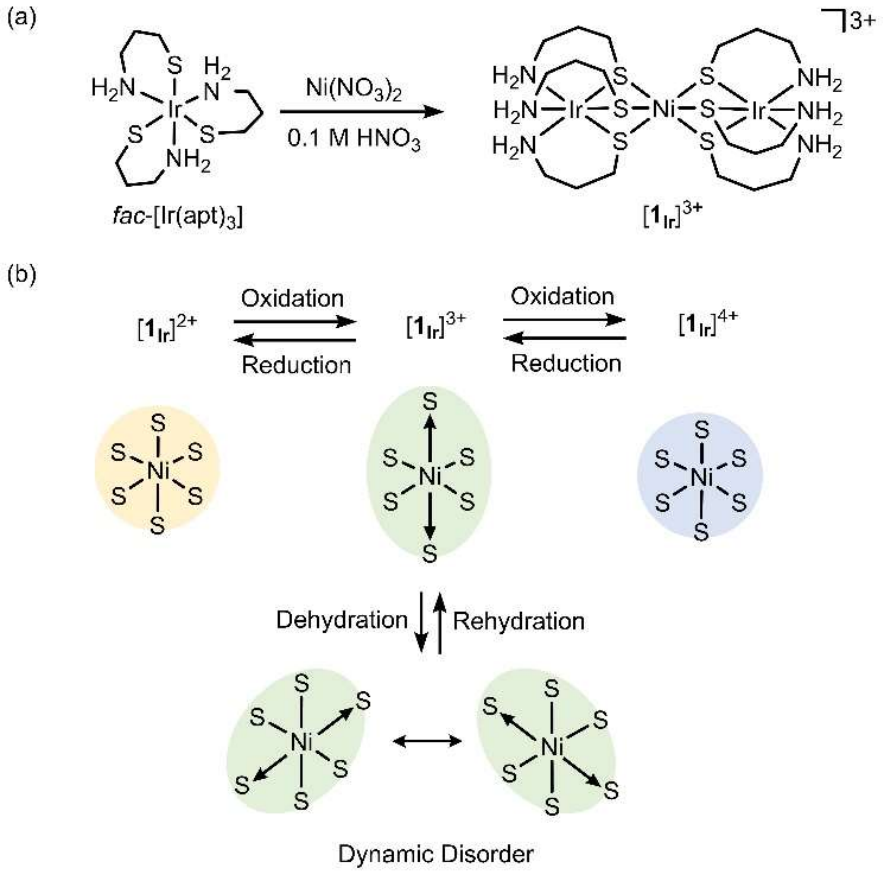

Scheme 1. (a) Synthetic route of $[\mathbf{1}_{\mathbf{Ir}}]^{3+}$ from *fac*-[Ir(apt)$_3$] and Ni^{2+}. (b) Interconversion of the structures of a Ni^{III} center in $[\mathbf{1}_{\mathbf{Ir}}]^{3+}$ by oxidation/reduction and dehydration/rehydration.

Results and Discussion

An off-white powder of *fac*-[Ir(apt)$_3$], which is insoluble in water, was synthesized by the reaction of $IrCl_3 \cdot 3H_2O$ with excess Hapt and NaOH in degassed, refluxing water. Its structure was confirmed by IR spectroscopy and its powder X-ray diffraction pattern, which are similar to those

of *fac*-[Rh(apt)$_3$] (Figures S1 and S2),[25] together with elemental analysis. Subsequently, an off-white aqueous suspension of *fac*-[Ir(apt)$_3$] was treated with 0.5 mol equiv of Ni(NO$_3$)$_2$·6H$_2$O, which gave a clear orange reaction solution. The reaction solution became dark purple in color on adding 0.1 M aqueous HNO$_3$, from which black plate crystals ([**1**$_{\mathbf{Ir}}$](NO$_3$)$_3$·2H$_2$O) were isolated by adding aqueous NaNO$_3$. X-ray fluorescence spectrometry indicated that [**1**$_{\mathbf{Ir}}$](NO$_3$)$_3$·2H$_2$O contains Ni and Ir atoms in a 1:2 ratio (Figure S3). The absorption spectrum of [**1**$_{\mathbf{Ir}}$]$^{3+}$ is characterized by several broad bands in the visible region (Figure 1). This spectral feature corresponds well with that of the previously reported [Ni{Rh(apt)$_3$}$_2$]$^{3+}$ ([**1**$_{\mathbf{Rh}}$]$^{3+}$), in which two *fac*-[Rh(apt)$_3$] units are spanned by a Ni^{III} ion through sulfur bridges, although each band for [**1**$_{\mathbf{Ir}}$](NO$_3$)$_3$ appears at a longer wavelength than for [**1**$_{\mathbf{Rh}}$](NO$_3$)$_3$ (Figure S4).

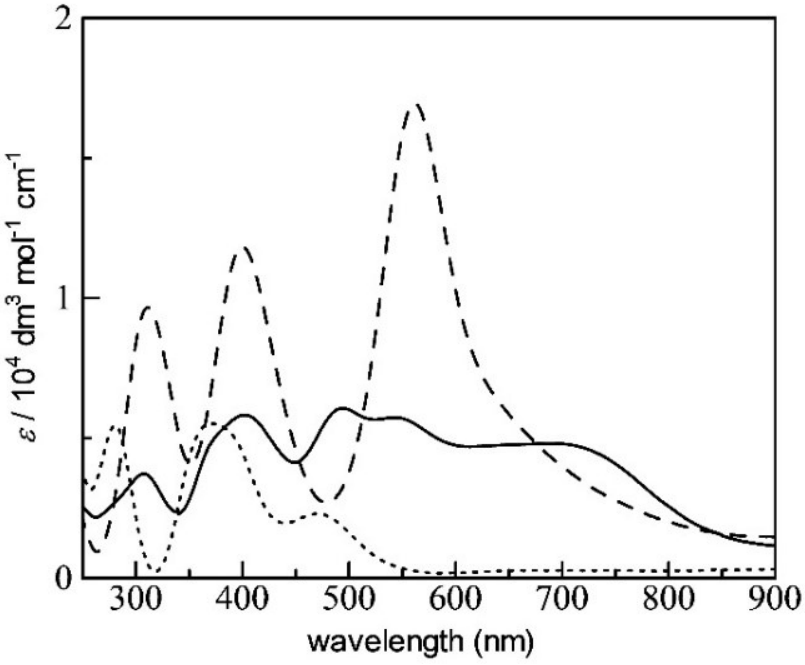

Figure 1. Absorption spectra of [**1**$_{\mathbf{Ir}}$]$^{2+}$ (dotted line), [**1**$_{\mathbf{Ir}}$]$^{3+}$ (solid line), and [**1**$_{\mathbf{Ir}}$]$^{4+}$ (dashed line) in 0.01 M aqueous HNO$_3$.

The structure of $[\mathbf{1_{Ir}}](NO_3)_3$ was established by single-crystal X-ray crystallography at 100 K (Table S1). The X-ray analysis revealed that $[\mathbf{1_{Ir}}](NO_3)_3 \cdot 2H_2O$ contains complex cations and nitrate anions in a 1:3 ratio, along with water molecules of crystallization (Figure S5), indicating the tri-cationic nature of the complex cation. The complex cation $[\mathbf{1_{Ir}}]^{3+}$ has an S-bridged trinuclear structure with a C_s symmetry, in which a nickel center is surrounded by six thiolato S atoms from two terminal *fac*-[Ir(apt)$_3$] units (Figure 2 and Table S2). Of the six Ni-S bonds, two of them in axis C (Ni1-S3 = 2.462 Å) are appreciably longer than those of the other bonds in axes A and B (Ni1-S1 = 2.289 Å, Ni1-S2 = 2.327 Å). A similar structural feature has been observed for $[\mathbf{1_{Rh}}]^{3+}$, which has been ascribed to a Jahn-Teller distortion for nickel(III) center with a low-spin d^7 electronic configuration (Figure S6).[25] Thus, the nickel center in $[\mathbf{1_{Ir}}]^{3+}$ is assumed to have a formal oxidation state of +III, as in the case of $[\mathbf{1_{Rh}}]^{3+}$, considering its EPR spectrum and magnetic susceptibility data (Figures S7 and S8). However, the Jahn-Teller elongation in $[\mathbf{1_{Ir}}]^{3+}$ is less significant than that in $[\mathbf{1_{Rh}}]^{3+}$ (Ni1-S1 = 2.269 Å, Ni1-S2 = 2.302 Å, Ni1-S3 = 2.458 Å).

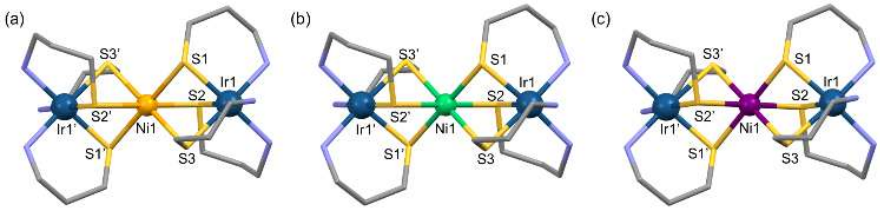

Figure 2. X-ray structures of (a) $[\mathbf{1_{Ir}}]^{2+}$, (b) $[\mathbf{1_{Ir}}]^{3+}$, and (c) $[\mathbf{1_{Ir}}]^{4+}$.

The cyclic voltammogram (CV) of $[\mathbf{1_{Ir}}]^{3+}$ in 0.01 M aqueous HNO_3 shows reversible one-electron redox processes in the oxidative and reductive scans (Figure 3). The half-wave potential ($E_{1/2}$) of the reduction process is –0.05 V vs. Ag/AgCl, which is more negative than that for $[\mathbf{1_{Rh}}]^{3+}$ ($E_{1/2}$ = +0.03 V). This is also the case for the oxidation process; the $E_{1/2}$ values for $[\mathbf{1_{Ir}}]^{3+}$ and $[\mathbf{1_{Rh}}]^{3+}$ are +0.30 V and +0.42 V, respectively. Thus, *fac*-[Ir(apt)$_3$] stabilizes the higher oxidation states of the

nickel center more than *fac*-[Rh(apt)$_3$]. This result is unexpected because the $Co^{III/II}$ redox potential for [Co{Ir(2-aminoethanethiolate)$_3$}$_2$]$^{3+}$ (–0.23 V) is more positive than that for [Co{Rh(2-aminoethanethiolate)$_3$}$_2$]$^{3+}$ (–0.36 V) due to the weaker electron donation of thiolato groups in *fac*-[Ir(2-aminoethanethiolate)$_3$] compared with those in *fac*-[Rh(2-aminoethanethiolate)$_3$].[32]

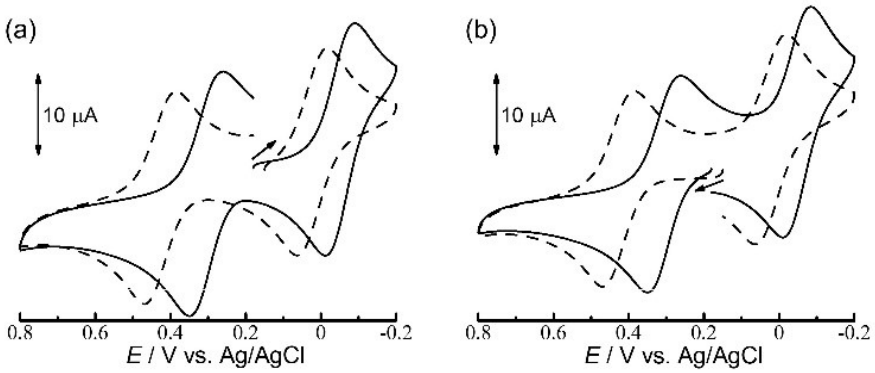

Figure 3. Cyclic voltammogram of [**1**$_{\mathbf{Ir}}$]$^{3+}$ (solid line) and [**1**$_{\mathbf{Rh}}$]$^{3+}$ (dashed line) in 0.01 M aqueous HNO_3 with a scan rate 0.1 Vs^{-1}: (a) reductive scan and (b) oxidative scan.

The absorption spectra of the one-electron reduced and oxidized species of [**1**$_{\mathbf{Ir}}$]$^{3+}$ ([**1**$_{\mathbf{Ir}}$]$^{2+}$ and [**1**$_{\mathbf{Ir}}$]$^{4+}$) were obtained by means of spectroelectrochemistry. (Figures 1 and S9). As expected, the overall spectral features of [**1**$_{\mathbf{Ir}}$]$^{2+}$ and [**1**$_{\mathbf{Ir}}$]$^{4+}$ resemble those of the corresponding [**1**$_{\mathbf{Rh}}$]$^{2+}$ and [**1**$_{\mathbf{Rh}}$]$^{4+}$ having Ni^{II} and Ni^{IV} centers, respectively (Figure S3). Based on the TD-DFT calculation (Figure S10 and Tables S3-S8), all the characteristic absorption bands for [**1**$_{\mathbf{Ir}}$]$^{2+}$ and [**1**$_{\mathbf{Ir}}$]$^{3+}$ are assignable to the charge transfer from sulfur to iridium with a minor contribution due to the charge transfer from iridium to nickel. For [**1**$_{\mathbf{Ir}}$]$^{4+}$, the characteristic absorption band at 311 nm is assignable to the charge transfer from sulfur to nickel, while the absorption bands at 400 nm and 562 nm are assignable to the charge transfer from iridium to nickel. Compounds [**1**$_{\mathbf{Ir}}$]$^{2+}$ and [**1**$_{\mathbf{Ir}}$]$^{4+}$

were successfully isolated as their nitrate salts by treating $[\mathbf{1}_{\mathbf{Ir}}](NO_3)_3$ with $NaBH_4$ and $(NH_4)_2[Ce(NO_3)_6]$, respectively, according to similar procedures used for the synthesis of $[\mathbf{1}_{\mathbf{Rh}}]^{2+}$ and $[\mathbf{1}_{\mathbf{Rh}}]^{4+}$ from $[\mathbf{1}_{\mathbf{Rh}}](NO_3)_3$.[25] The structures of $[\mathbf{1}_{\mathbf{Ir}}](NO_3)_2\cdot 4H_2O$ and $[\mathbf{1}_{\mathbf{Ir}}](NO_3)_4\cdot 5H_2O$ were also determined by single-crystal X-ray crystallography (100 K). The complex cation in $[\mathbf{1}_{\mathbf{Ir}}](NO_3)_2$ and $[\mathbf{1}_{\mathbf{Ir}}](NO_3)_4$ has the same S-bridged trinuclear structure as that of $[\mathbf{1}_{\mathbf{Ir}}]^{3+}$ (Figure 2 and Table S2). However, $[\mathbf{1}_{\mathbf{Ir}}](NO_3)_2$ and $[\mathbf{1}_{\mathbf{Ir}}](NO_3)_4$ contain complex cations and nitrate anions in 1:2 and 1:4 ratios, respectively (Figure S5). In addition, the nickel center in each of $[\mathbf{1}_{\mathbf{Ir}}]^{2+}$ and $[\mathbf{1}_{\mathbf{Ir}}]^{4+}$ adopts an almost regular octahedral geometry with the lack of a Jahn-Teller distortion unlike the nickel center in $[\mathbf{1}_{\mathbf{Ir}}]^{3+}$ (Table S2). The averaged Ni-S bond distances in $[\mathbf{1}_{\mathbf{Ir}}]^{2+}$ and $[\mathbf{1}_{\mathbf{Ir}}]^{4+}$ are 2.432 Å and 2.299 Å, which are in agreement with those in $[\mathbf{1}_{\mathbf{Rh}}]^{2+}$ (2.418 Å) and $[\mathbf{1}_{\mathbf{Rh}}]^{4+}$ (2.274 Å), respectively.[25]

To gain insight into the more negative redox potentials for $[\mathbf{1}_{\mathbf{Ir}}]^{3+}$ compared to those for $[\mathbf{1}_{\mathbf{Rh}}]^{3+}$, DFT calculations were performed for $[\mathbf{1}_{\mathbf{Ir}}]^{n+}$ and $[\mathbf{1}_{\mathbf{Rh}}]^{n+}$ (n = 2, 3, 4) at the B3LYP level using the LANL2DZ basis. Their optimized structures compare well with the corresponding X-ray structures of $[\mathbf{1}_{\mathbf{Ir}}]^{n+}$ and $[\mathbf{1}_{\mathbf{Rh}}]^{n+}$ (Tables S9 and S10). The Jahn-Teller distortion of the nickel center in $[\mathbf{1}_{\mathbf{Ir}}]^{3+}$, which is smaller than that in $[\mathbf{1}_{\mathbf{Rh}}]^{3+}$, is also reproduced in the optimized structures. Notably, the atomic orbitals of the two terminal iridium centers largely contribute to the α-HOMO in the optimized structure of $[\mathbf{1}_{\mathbf{Ir}}]^{3+}$ (13%), while the contribution due to the rhodium centers (7%) is much smaller in the optimized structure of $[\mathbf{1}_{\mathbf{Rh}}]^{3+}$ (Figure S11). The spin density distribution at the Ir center is also larger than that at the Rh center (Figure S12). Thus, the electron spin on the nickel center in $[\mathbf{1}_{\mathbf{Ir}}]^{3+}$ is partially delocalized with the iridium centers through sulfur bridges, which is responsible for the more negative redox potentials for $[\mathbf{1}_{\mathbf{Ir}}]^{3+}$. It is considered that such a delocalization through sulfur bridges does not take place for $[Co\{Ir(2\text{-aminoethanethiolate})_3\}_2]^{3+}$

because the S–Ir–S angles of *fac*-[Ir(2-aminoethanethiolate)$_3$] with five-membered N,S-chelate rings are much larger and are disadvantageous for chelating to a metal center with overlapping sulfur orbitals,[25,27,28,29] leading to the more positive $Co^{III/II}$ redox potential for [Co{Ir(2-aminoethanethiolate)$_3$}$_2$]$^{3+}$ compared with the potential for [Co{Rh(2-aminoethanethiolate)$_3$}$_2$]$^{3+}$ due to the weaker electron donating nature of thiolato groups in *fac*-[Ir(2-aminoethanethiolate)$_3$].[32]

To further prove the oxidation state of the nickel center in [**1**$_{\mathbf{Ir}}$]$^{n+}$, the X-ray absorption fine structure (XAFS) measurements were carried out at room temperature. The Ni L_3-edge ($2p_{3/2}\rightarrow 3d$) absorption bands shift to higher energy in the order [**1**$_{\mathbf{Ir}}$]$^{2+}$ (854.2 eV) < [**1**$_{\mathbf{Ir}}$]$^{3+}$ (855.0 eV) < [**1**$_{\mathbf{Ir}}$]$^{4+}$ (855.6 eV), indicative of the increase of the oxidation number of the nickel centers in this order (Figure S13). The same trend has been observed for the Ni L_3-edge absorption bands for [**1**$_{\mathbf{Rh}}$]$^{n+}$; [**1**$_{\mathbf{Rh}}$]$^{2+}$ (854.4 eV) < [**1**$_{\mathbf{Rh}}$]$^{3+}$ (854.8 eV) < [**1**$_{\mathbf{Rh}}$]$^{4+}$ (855.4 eV).[24] Of note is that the Ir M_3-edge ($3p_{3/2} \rightarrow 5d$) absorption bands of [**1**$_{\mathbf{Ir}}$]$^{n+}$ shift slightly to higher energy with increasing the molecular charges; [**1**$_{\mathbf{Ir}}$]$^{2+}$ (2552.6 eV) < [**1**$_{\mathbf{Ir}}$]$^{3+}$ (2552.8 eV) < [**1**$_{\mathbf{Ir}}$]$^{4+}$ (2553.0 eV). This is in contrast to the constant energy of the Rh M-edge absorption bands for [**1**$_{\mathbf{Rh}}$]$^{n+}$.[24] From these results, together with the DFT calculations, we conclude that there exists the valence charge delocalization between the nickel and iridium centers in [**1**$_{\mathbf{Ir}}$]$^{n+}$, which is indicative of the redox non-innocent nature of the metalloligand *fac*-[Ir(apt)$_3$]. This conclusion is compatible with the Jahn-Teller distortion of the nickel center found in the X-ray structure of [**1**$_{\mathbf{Ir}}$]$^{3+}$, which is less significant than that in [**1**$_{\mathbf{Rh}}$]$^{3+}$.

The thermal stability of [**1**$_{\mathbf{Ir}}$]$(NO_3)_3$ was investigated by TG-DTA measurements (Figure S14). While [**1**$_{\mathbf{Ir}}$]$(NO_3)_3$ shows an endothermic peak due to the removal of lattice water molecules at around 70°C, no significant thermal decomposition is observed until 200°C. Such a high thermal

stability is remarkable for nickel(III) coordination species. Thanks to the high stability of [**1**$_{\mathbf{Ir}}$](NO$_3$)$_3$, we were able to determine its structure at high temperature by single-crystal X-ray crystallography (Table S11). Consistent with the TG-DTA analysis, the structure of [**1**$_{\mathbf{Ir}}$](NO$_3$)$_3$ at 400 K does not contain lattice water molecules due to dehydration, although its overall structure is essentially the same as that at 100 K (Figure S15). It should be noted that the crystallographic Jahn-Teller distortion of the Ni^{III} center in [**1**$_{\mathbf{Ir}}$](NO$_3$)$_3$ at 400 K is distinct from that at 100 K (Figure 4). That is, the longer Ni-S bonds on the Jahn-Teller distortion axis become shorter from 2.462 Å at 100 K to 2.393 Å at 400 K with the elongation of the Ni-S bonds on another axis (A) from 2.289 Å at 100 K to 2.375 Å at 400 K, while the Ni-S bonds on the remaining axis (B) are almost constant (2.327 Å at 100 K, 2.323 Å at 400 K). Such a temperature dependence is characteristic of dynamic disorder of a Jahn-Teller distortion at the nickel(III) ion.

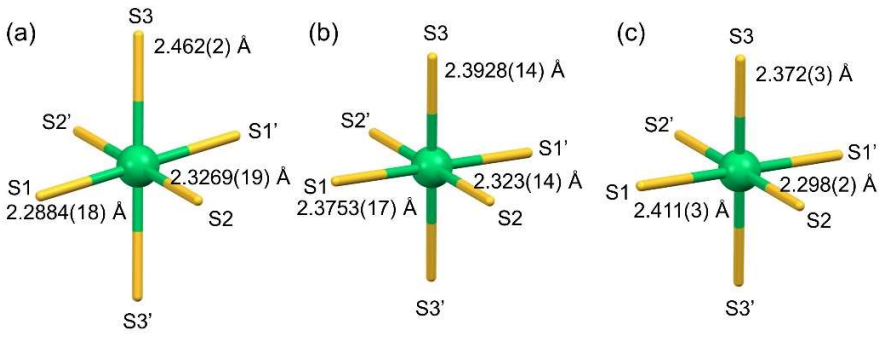

Figure 4. X-ray structures of a Ni^{III} center in (a) [**1**$_{\mathbf{Ir}}$](NO$_3$)$_3$ at 100 K, (b) the dehydrated [**1**$_{\mathbf{Ir}}$](NO$_3$)$_3$ at 400 K, and (c) the dehydrated [**1**$_{\mathbf{Ir}}$](NO$_3$)$_3$ at 100 K.

The existence of masked disorder in the Ni-S bonds of the dehydrated crystal was confirmed by mean-square displacement ellipsoid (MSDA) calculations from the crystal structures.[33] The difference between the MSDAs of the two atoms in a bond, $<d^2>$, indicates the degree of libration within that bond. That is a useful fingerprint for the presence or absence of unresolved structural disorder about a Jahn-Teller-active metal ion.[30] In [**1**$_{\mathbf{Ir}}$]$(NO_3)_3 \cdot 2H_2O$ at 100 K, $<d^2>$ for the Ni-S bonds is 21(9)-64(9) x10^{-4} Å^2 which are equal within 4 esds, and the same order of magnitude as the Ir-S bonds in the molecule [9(8)-27(8) x10^{-4} Å^2] (Table S12). That is consistent with a static Jahn-Teller elongation in that crystal, as predicted from the Ni-S distances (Figure 4). In contrast, dehydrated [**1**$_{\mathbf{Ir}}$]$(NO_3)_3$ at the same temperature shows $<d^2>$ = 172(15) x10^{-4} Å^2 [Ni1-S1], 52(14) [Ni1-S2] and 165(15) [Ni1-S3]. The larger internal libration within the two longer Ni–S bonds is characteristic of a Jahn-Teller elongation that is disordered over the S1-Ni1-S1' and S3-Ni1-S3' axes.[30,31] This disorder is not reflected in the Ir-S bonds however, whose $<d^2>$ values are all still equal within experimental error (Table S12).

The temperature dependence of the Ni1-S1 bonds implies the Jahn-Teller disorder is dynamic in nature.[30] Intriguingly, the structure at 100 K implies the minimum energy orientation for the Jahn-Teller elongation in the anhydrous crystals is the S1-Ni1-S1' axis, which is rotated with respect to the static elongation along S3-Ni1-S3' in [**1**$_{\mathbf{Ir}}$]$(NO_3)_3 \cdot 2H_2O$.[34,35] Measurements at helium temperatures where the disorder should be frozen out, would be required to confirm that observation.[36]

To confirm that the origin of the change in the Jahn-Teller distortion is due to the dehydration, rather than the temperature change, X-ray datasets from a crystal [**1**$_{\mathbf{Ir}}$]$(NO_3)_3 \cdot 2H_2O$ were collected at 353 K every 6 min for 30 min (Table S13 and Figure S16). No degradation of the crystal was

detected during the measurements, and the crystal structures after 6 min and 12 min are the same as the initial structure. On the other hand, no water molecules are present in the structure after 18 min, and its structure is almost the same as that obtained by heating the original crystal at 400 K. The dehydrated structure after 18 min is the same as that after 30 min. Subsequently, the dehydrated crystals were allowed to stand under humidified conditions for 1 h. The powder X-ray diffraction measurements showed that the rehydrated sample has the same structure as that found in the original hydrated structure (Figure S17).

A detailed inspection of the crystal structure of $[\mathbf{1_{Ir}}](NO_3)_3 \cdot 2H_2O$ revealed that the complex cations are tightly hydrogen-bonded not only with nitrate anions but also with water molecules of crystallization through the apt amine groups in the original hydrated structure (Figure S18). In the dehydrated structure, several NH···O hydrogen bonds are cleaved due to the removal of water molecules, which is most likely responsible for converting the Jahn-Teller distortion of the Ni^{III} center in $[\mathbf{1_{Ir}}]^{3+}$. It is noticed that each apt ligand of the *fac*-$[Ir(apt)_3]$ unit in $[\mathbf{1_{Ir}}](NO_3)_3$ forms a shorter Ni-S bond when its amine group forms multiple NH···O hydrogen bonds. Hence, the loss of these hydrogen bonds, which are remote from the nickel center, influences the lability of the Ni-S bonds on dehydration. In contrast to the Ni^{III} center, no significant structural change was observed for the Ir^{III} center after dehydration. This is compatible with the fact that the Ir^{III} center with the low-spin d^6 electronic configuration is commonly structurally rigid in contrast to the Ni^{III} center with the low-spin d^7 electronic configuration.

Conclusion

In this study, the S-bridged trinuclear complex $[Ni\{Ir(apt)_3\}_2]^{3+}$ ($[\mathbf{1_{Ir}}]^{3+}$) was successfully synthesized and isolated by using the newly prepared *fac*-$[Ir(apt)_3]$ as an S-donating metalloligand. $[\mathbf{1_{Ir}}]^{3+}$ showed two reversible one-electron redox couples, which appeared at more negative potentials than those for $[Ni\{Rh(apt)_3\}_2]^{3+}$ ($[\mathbf{1_{Rh}}]^{3+}$). Thus, the higher oxidation states of nickel center were more stabilized by using *fac*-$[Ir(apt)_3]$ instead of *fac*-$[Rh(apt)_3]$. The structure of $[\mathbf{1_{Ir}}]^{3+}$, together with its reduced and oxidized species ($[\mathbf{1_{Ir}}]^{2+}$ and $[\mathbf{1_{Ir}}]^{4+}$), was established by single-crystal X-ray crystallography. The elongation-type Jahn-Teller distortion of Ni^{III} center was observed for $[\mathbf{1_{Ir}}]^{3+}$, although the distortion is less significant than that found in $[\mathbf{1_{Rh}}]^{3+}$. The more negative potentials and the less significant Jahn-Teller distortion were attributed to the partial delocalization of an electronic spin between the nickel and iridium centers in $[\mathbf{1_{Ir}}]^{3+}$.

$[\mathbf{1_{Ir}}]^{3+}$ was stable even at a high temperature, which allowed us to determine its dehydrated crystal structure. Dehydration affects the dynamics of the crystal, as evidenced by the onset of Jahn-Teller disorder at the Ni^{III} ion. Hydrogen-bonding between the apt amine groups of $[\mathbf{1_{Ir}}]^{3+}$ and nitrate anions/water molecules, which is modified by dehydration, accounts for the appearance of this Jahn-Teller disorder in the solid state. Intriguingly, there is evidence that dehydration of the crystal leads to reorientation of the minimum energy Jahn-Teller distortion in $[\mathbf{1_{Ir}}]^{3+}$. While thermally or pressure-induced reorientation of Jahn-Teller distortion axes is known in a small number of molecular copper(II) compounds,[34,35] this is the first example of reorientation of Jahn-Teller distortion axes induced by desolvation.

Finally, these results have revealed the tuning of the redox property and Jahn-Teller dynamics of a Ni^{III} center by changing a metal center in its coordinated metalloligands. This should contribute to the future development of research fields that involve high-valent metal centers.

Experimental Methods

Material. 3-Aminopropanethiol hydrochloride was prepared according to procedures described in the literature.[25]

Preparation of *fac*-[Ir(apt)$_3$]. To a colorless solution containing 6.3 g (49 mmol) of 3-aminopropanethiol hydrochloride in 50 ml of degassed water was added 3.8 g (95 mmol) of NaOH. To the resulting colorless solution was added 2.7 g (7.7 mmol) of $IrCl_3 \cdot 3H_2O$. The mixture was then refluxed at 120°C for 4 h under a nitrogen atmosphere. The resulting white suspension was cooled to room temperature overnight and then filtered to collect an off-white powder. The off-white powder was washed with water, EtOH, and acetone. Yield: 1.5 g (42%).

Anal. [Ir(apt)$_3$]: Calcd for [Ir(apt)$_3$]·0.5H_2O = $C_9H_{25}Ir_1N_3O_{0.5}S_3$ = C, 22.92; H, 5.34; N, 8.91%. Found: C, 23.11; H, 4.99; N, 8.62%. IR spectrum (cm^{-1}, KBr disk): 3435 (ν_{OH}), 3241 (ν_{NH2}), 3136(ν_{NH2}), 2927 (ν_{CH2}), 1626 (ν_{COOH}), 1391 (δ_{CH2}).

Preparation of [Ni{Ir(apt)$_3$}$_2$](NO$_3$)$_3$ ([1$_{Ir}$](NO$_3$)$_3$). To an off-white suspension containing *fac*-[Ir(apt)$_3$] (300 mg, 0.65 mmol) in 80 ml of water was added $Ni(NO_3)_2 \cdot 6H_2O$ (98 mg, 0.34 mmol). The mixture was stirred at 50°C for 1 h, which yielded an orange solution. To this solution was added 24 ml of an aqueous solution of 0.1 M nitric acid, followed by further stirring at 50°C overnight. After filtration, 30 ml of a saturated aqueous solution of sodium nitrate was added to the resulting dark purple solution. Slow evaporation at room temperature yielded black plate crystals of [**1$_{Ir}$**](NO$_3$)$_3$ suitable for single-crystal X-ray analysis, which were collected by filtration. Yield: 83 mg (21%).

Anal. [**1$_{Ir}$**](NO$_3$)$_3$: Calcd for [Ni{Ir(apt)$_3$}$_2$](NO$_3$)$_3$·2H_2O = $C_{18}H_{52}Ir_2N_9Ni_1O_{11}S_6$ = C, 17.92; H, 4.35; N, 10.45%. Found: C, 17.92; H, 4.22; N, 10.56%. IR spectrum (cm^{-1}, KBr disk): 3173 (ν_{NH2}),

3098 (ν_{NH2}), 2922 (ν_{CH2}), 1599 (δ_{NH2}), 1385 (ν_{NO3}). UV-Vis absorption in 0.01 M nitric acid (λ_{max}/nm, (ε/mol^{-1}dm^{3}cm^{-1})): 699(4800), 543(5740), 494(6070), 402(5820), 308(3720).

Preparation of [Ni{Ir(apt)$_3$}$_2$](NO$_3$)$_2$ ([1$_{Ir}$](NO$_3$)$_2$). To a purple solution containing [**1**$_{Ir}$](NO$_3$)$_3$ (50 mg, 0.041 mmol) in 30 ml of water was added a solid sample of sodium borohydride (17 mg, 0.45 mmol), which immediately yielded an orange suspension. After the mixture was stirred at room temperature for several minutes, 5 ml of saturated aqueous sodium nitrate was added. After stirring at room temperature for 30 min, an orange powder of [**1**$_{Ir}$](NO$_3$)$_2$ was collected by filtration and washed with water, ethanol, and diethyl ether. Yield: 36 mg (76%). Single-crystals suitable for X-ray analysis were obtained by the following procedure: To an off-white suspension containing *fac*-[Ir(apt)$_3$] (10 mg, 0.022 mmol) in 30 ml of degassed water was added a solid sample of Ni(NO$_3$)$_2$·6H$_2$O (4.4 mg, 0.015 mmol), which immediately yielded an orange suspension. After the mixture was stirred at room temperature for 5 minutes, the suspension was filtrated. To the orange solution wad added 0.1 ml of saturated aqueous solution of sodium nitrate. The mixture was allowed to stand in a refrigerator for 18 days, yielding orange block crystals of [**1**$_{Ir}$](NO$_3$)$_2$ suitable for single-crystal X-ray analysis.

Anal. [**1**$_{Ir}$](NO$_3$)$_2$: Calcd for [Ni{Ir(apt)$_3$}$_2$](NO$_3$)$_2$·3H$_2$O = C$_{18}$H$_{54}$Ir$_2$N$_8$NiO$_9$S$_6$: C, 18.60; H, 4.68; N, 9.64 %. Found: C, 18.65; H, 4.50; N, 9.70 %. IR spectrum (cm^{-1}, KBr disk): 3207 (ν_{NH2}), 3125 (ν_{NH2}), 2924 (ν_{CH2}), 1601 (δ_{NH2}), 1384 (ν_{NO3-}). UV-Vis absorption in 0.01 M nitric acid (λ_{max}/nm, (ε/mol^{-1}dm^{3}cm^{-1})): 473(2300), 370(5540), 281(5470).

Preparation of [Ni{Ir(apt)$_3$}$_2$](NO$_3$)$_4$ ([1$_{Ir}$](NO$_3$)$_4$). To a purple solution containing [**1**$_{Ir}$](NO$_3$)$_3$ (20 mg, 0.017 mmol) in 2 ml of 0.1 M aqueous nitric acid was added a solid sample of cerium ammonium nitrate (19 mg, 0.035 mmol), followed by stirring at room temperature for 20 min. To the resulting dark blue-purple solution were added 5 ml of ethanol and 10 ml of diethyl ether,

which gave a black crystalline powder of [**1**$_{\mathbf{Ir}}$]$(NO_3)_4$ after 15 min. This crystalline powder was filtered and washed with diethyl ether. Yield: 10 mg (44%). Single-crystals suitable for X-ray analysis were obtained by the following procedure: To a purple solution containing [**1**$_{\mathbf{Ir}}$]$(NO_3)_3$ (5.3 mg, 4.39 μmol) in 5 ml of 0.01 M aqueous nitric acid was added a solid sample of cerium ammonium nitrate (13 mg, 0.024 mmol), followed by stirring at room temperature for 5 min. To the resulting dark blue-purple solution was added 5 ml of saturated aqueous solution of sodium nitrate. The mixture was allowed to stand in at refrigerator overnight, yielding black plate crystals of [**1**$_{\mathbf{Ir}}$]$(NO_3)_4$ suitable for single-crystal X-ray analysis.

Anal. [**1**$_{\mathbf{Ir}}$]$(NO_3)_4$: Calcd for $[Ni\{Ir(apt)_3\}_2](NO_3)_4 \cdot 6.5H_2O = C_{18}H_{61}Ir_2N_{10}NiO_{18.5}S_6$: C, 16.02; H, 4.56; N, 10.38 %. Found: C, 15.73; H, 4.18; N, 10.01 %. IR spectrum (cm^{-1}, KBr disk): 3133 (ν_{NH2}), 3083 (ν_{NH2}), 2953 (ν_{CH2}), 1599 (δ_{NH2}), 1384 (ν_{NO3-}). ^{1}H NMR spectrum (ppm from DSS, 1 M DNO_3): 5.62 (1H, d, J = 11.2 Hz), 4.79 (1H, t, J = 11.0 Hz), 3.38-3.28 (1H, m), 3.18-3.11 (1H, m), 2.94 (1H, dd, J_1 = 14.0 Hz, J_2 = 6.0 Hz), 2.72 (1H, t, J = 12.8 Hz), 2.48-2.39 (1H, m), 2.14-2.03 (1H, m). UV-Vis absorption in 0.01 M nitric acid (λ_{max}/nm, (ε/$mol^{-1}dm^3cm^{-1}$)): 562(17000), 400(11800), 311 (9670).

Physical measurements. The IR spectra in the range of 4000-400 cm^{-1} were measured on a JASCO FT/IR-4100 spectrometer by using KBr method at room temperature. Elemental analyses (C, H, N) were performed at Osaka University using YANACO MT-6. TG-DTA measurements were performed on a SHIMADZU DTG60 under N_2 gas flow (50 mL/min) using Al_2O_3 as a reference with the scan rate of 5.0 °C/min. EPR spectrum was recorded in water/ethylene glycol (1:1) glass at 103 K with a JEOL JES-FA200 instrument. Absorption spectra were recorded on a JASCO V-670 UV/VIS spectrometer at room temperature. High-quality powder X-ray diffraction (PXRD) was performed at room temperature in transmission mode (synchrotron radiation λ = 1.0

Å; 2θ range = 2–78°; step width = 0.01°; data collection time 1 min) on a diffractometer equipped with a MYTHEN microstrip X-ray detector (Dectris Ltd) at the SPring-8 BL02B2 beamline. X-ray fluorescence analyses were performed on a SHIMADZU EDX-900 spectrometer. Magnetic measurements were carried out using a Quantum-Design MPMS XL7AC SQUID magnetometer. The observed magnetic moment data were corrected for the diamagnetic contribution (χ_{dia}) by the equation $\chi_{dia} = -1/2 \times M \times 10^{-6}$ emu/mol.

X-ray crystal structure determination. Diffraction data for [$\mathbf{1_{Ir}}$]$(NO_3)_2$ and [$\mathbf{1_{Ir}}$]$(NO_3)_4$ were recorded on a Rigaku R-AXIS VII imaging plate diffractometer with graphite-monochromated Mo-Kα radiation. Diffraction data for [$\mathbf{1_{Ir}}$]$(NO_3)_3$, temperature dependent X-ray structures of [$\mathbf{1_{Ir}}$]$(NO_3)_3$, and time dependent X-ray structures of [$\mathbf{1_{Ir}}$]$(NO_3)_3$ were recorded on a Rayonix MX225HS CCD area detector with synchrotron radiation (λ = 0.6300 Å) at the 2D beamline at the Pohang Accelerator Laboratory (PAL). The intensity data were processed using the HKL3000 program and collected by using the ω-scan technique. The structures were solved by direct methods using SHELXS-2014.[37] Structure refinements were carried out using the full-matrix least squares (SHELXL-2018/3).[37] Hydrogen atoms were included in the calculated positions except for those from water molecules. For [$\mathbf{1_{Ir}}$]$(NO_3)_2$, SIMU and ISOR were applied for disordered parts of organic ligands.[37] Several reflections which showed outliers ((I_{obs}-I_{calc})/Sigma(W) > 10) were omitted. For [$\mathbf{1_{Ir}}$]$(NO_3)_3$, DFIX and DANG were applied to model water molecules.[37] For [$\mathbf{1_{Ir}}$]$(NO_3)_4$, DFIX and DANG were applied to model water molecules. Several reflections which showed outliers ((I_{obs}-I_{calc})/Sigma(W) > 10) were omitted.[37]

Mean square displacement ellipsoid calculations were performed using *PLATON*.[38]

Electrochemical experiments. Cyclic voltammetric (CV) measurements were performed at room temperature using an ALS/CHI-720ES voltammetric analyzer. The working, reference, and

counter electrodes were a glassy carbon disk electrode (ϕ 1.8 mm), a reference Ag/AgCl electrode (3.0 M NaCl aq.), and a platinum wire, respectively. Sample solutions were prepared at a concentration of 1.0 mM in 0.01 M aqueous HNO_3. The CV of [**1**$_{\mathbf{Ir}}$]$(NO_3)_3$ exhibited a single redox couple at $E_{1/2}$ = -0.05 V (vs. Ag/AgCl) in the negative scan starting from +0.18 V (Figure 3). The peak currents were proportional to the square root of the scan rates, and the ratio of anodic to cathodic peak currents was nearly unity with a peak separation (ΔE_p) of 89 mV at a scan rate of 100 mV s^{-1}. These results imply that the redox process at $E_{1/2}$ = -0.05 V is a reversible, one-electron event. The CV in the positive scan exhibited a single redox couple at $E_{1/2}$ = +0.30 V (Figure 3). This process is also characterized as a reversible, one-electron event based on analysis of the peak currents and peak separation (ΔE_p = 89 mV). Spectroelectrochemical experiments were performed using a thin-layer quartz cell (0.5 mm light path length) with a Pt-mesh (100 mesh) working electrode, an aqueous Ag/AgCl/NaCl (3 M) reference electrode, and a Pt-wire auxiliary electrode.

DFT calculations. DFT and TD-DFT calculations for [**1**$_{\mathbf{Ir}}$]$^{2+}$, [**1**$_{\mathbf{Ir}}$]$^{3+}$, [**1**$_{\mathbf{Ir}}$]$^{4+}$, [**1**$_{\mathbf{Rh}}$]$^{2+}$, [**1**$_{\mathbf{Rh}}$]$^{3+}$, and [**1**$_{\mathbf{Rh}}$]$^{4+}$ were performed using the Gaussian 09 program[39] with the B3LYP functional. The LanL2DZ basis set was applied for all atoms. The initial structural parameters were taken from the single-crystal X-ray structures. The optimized structures with α-HOMO for [**1**$_{\mathbf{Ir}}$]$^{3+}$ and [**1**$_{\mathbf{Rh}}$]$^{3+}$ are displayed in Figure S11 and their structural parameters are summarized in Tables S9 and S10. The TD-DFT results are displayed in Figure S10 and Tables S3-S8.

XAFS measurements. XAFS measurements were carried out at BL-10 and BL-11 of the Synchrotron Radiation Center at Ritsumeikan University, Japan.[40,41] XAFS spectra were obtained in both partial fluorescence yield (PFY) mode and total electron yield (TEY) mode. Powder samples of [**1**$_{\mathbf{Ir}}$]$(NO_3)_2$, [**1**$_{\mathbf{Ir}}$]$(NO_3)_3$, and [**1**$_{\mathbf{Ir}}$]$(NO_3)_4$ were thinly spread on conductive carbon tape attached to the sample holder in air before transferring the samples to the vacuum chamber. We

repeatedly measured the spectra on the same and different sample positions to confirm the reproducibility of the data, and neither serious radiation damage nor a sample-position dependence of the XAFS spectra was observed. The measurements were performed at room temperature.

ASSOCIATED CONTENT

Supporting Information.

The following files are available free of charge. Infrared (IR), absorption, EPR spectra, powder X-ray diffraction patterns, X-ray crystal structures, HOMO structures, Ni L_3-edge and Ir M_3-edge XAS, and TG-DTA data are summarized in the Supporting Information (PDF).

Accession Codes

CCDC 2222064-2222075 contain the supplementary crystallographic data for this paper. These data can be obtained free of charge via www.ccdc.cam.ac.uk/data_request/cif, or by emailing data_request@ccdc.cam.ac.uk, or by contacting The Cambridge Crystallographic Data Centre, 12 Union Road, Cambridge CB2 1EZ, UK; fax: +44 1223 336033.

AUTHOR INFORMATION

Corresponding Author

* Takumi Konno

* konno@chem.sci.osaka-u.ac.jp.

* Nobuto Yoshinari

* nobuto@chem.sci.osaka-u.ac.jp.

* Naoto Kuwamura

* kuwamura@cc.kogakuin.ac.jp.

Author Contributions

M.K., N.K., and N.Y. performed the syntheses and characterization of the compounds; T. Kojima performed X-ray diffraction analysis; M.K. and M.A.H. performed all measurements related to the Jahn-Teller distortion; K.Y. and A.S. performed X-ray absorption spectra measurement and analysis. M.K., N.K., and T. Konno wrote the manuscript; T. Konno conceived and designed the project. All authors have given approval to the final version of the manuscript.

Funding Sources

This work was supported by JSPS KAKENHI (Grant Numbers 19K05667, 22K05286, 19K05496, and 20K05664).

ACKNOWLEDGMENT

Two of the authors (MK and KY) acknowledge Programs for Leading Graduate Schools: 'Interactive Material Science Cadet Program'. The synchrotron radiation experiments were performed at the BL02B2 beamline of SPring-8 with the approval of the Japan Synchrotron Radiation Research Institute (JASRI) (Proposal Nos. 2016A1485 and 2017B1203) and at 2D-SMC of the Pohang Accelerator Laboratory. The XAFS measurements were supported by the Project for Creation of Research Platforms and Sharing of Advanced Research Infrastructure, Japan

(Proposal Nos. S18004 and S18016). We thank Dr. Hiroki Wadati and Dr. Hirona Yamagishi (Synchrotron Radiation Center, Ritsumeikan University, Japan) for their support with the XAFS measurements.

REFERENCES

(1) Zheng, B.; Tang, F.; Luo, J.; Schultz, W.; Rath, N. P.; Mirica, L. M. Organometallic Nickel(III) Complexes Relevant to Cross-Coupling and Carbon–Heteroatom Bond Formation Reactions. *J. Am. Chem. Soc.* **2014**, *136*, 6499-6504.

(2) Zhang, S. K.; Struwe, J.; Hu, L.; Ackermann, L. Nickela-electrocatalyzed C−H Alkoxylation with Secondary Alcohols: Oxidation-Induced Reductive Elimination at Nickel(III). *Angew. Chem. Int. Ed.* **2020**, *59*, 3178-3183.

(3) Roberts, C. C.; Camasso, N. M.; Bowes, E. G.; Sanford, M. S. Impact of Oxidation State on Reactivity and Selectivity Differences between Nickel(III) and Nickel(IV) Alkyl Complexes. *Angew. Chem. Int. Ed.* **2019**, *58*, 9104-9108.

(4) Schultz, J. W.; Fuchigami, K.; Zheng, B.; Rath, N. P.; Mirica, L. M. Isolated Organometallic Nickel(III) and Nickel(IV) Complexes Relevant to Carbon–Carbon Bond Formation Reactions. *J. Am. Chem. Soc.* **2016**, *138*, 12928-12934.

(5) Pirovano, P.; Farquhar, E. R.; Swart, M.; McDonald, A. R. Tuning the Reactivity of Terminal Nickel(III)–Oxygen Adducts for C–H Bond Activation. *J. Am. Chem. Soc.* **2016**, *138*, 14362-14370.

(6) Watson, M. B.; Rath, N. P.; Mirica, L. M. Oxidative C–C Bond Formation Reactivity of Organometallic Ni(II), Ni(III), and Ni(IV) Complexes. *J. Am. Chem. Soc.* **2017**, *139*, 35-38.

(7) Zhou, W.; Schultz, J. W.; Rath, N. P.; Mirica, L. M.; Aromatic Methoxylation and Hydroxylation by Organometallic High-Valent Nickel Complexes. *J. Am. Chem. Soc.* **2015**, *137*, 7604-7607.

(8) Magallón, C.; Griego, L.; Hu, C. H.; Company, A.; Ribas, X.; Mirica, L. M. Organometallic Ni(II), Ni(III), and Ni(IV) complexes relevant to carbon–carbon and carbon–oxygen bond formation reactions. *Inorg. Chem. Front.* **2022,** *9*. 1016-1022.

(9) Na, H.; Watson, M. B.; Tang, F.; Rath, N. P.; Mirica, L. M. Photoreductive chlorine elimination from a Ni(III)Cl_2 complex supported by a tetradentate pyridinophane ligand. *Chem. Commun.* **2021**, *57*, 7264-7267.

(10) Alonso, P. J.; Arauzo, A. B.; García-Monforte, M. A.; Martín, A.; Menjón, B.; Rillo, C.; Tomás, M. Homoleptic Organoderivatives of High-Valent Nickel(III). *Chem. Eur. J.* **2009**, *15*, 11020-11030.

(11) Cho, J.; Kang, H. Y.; Liu, L. V.; Sarangi, R.; Solomon, E. I.; Nam, W. Mononuclear nickel(II)-superoxo and nickel(III)-peroxo complexes bearing a common macrocyclic TMC ligand. *Chem. Sci.* **2013**, *4*, 1502-1508.

(12) Chiou, T.-W.; Liaw, W.-F. Mononuclear Nickel(III) Complexes $[Ni^{III}(OR)(P(C_6H_3\text{-}3\text{-}SiMe_3\text{-}2\text{-}S)_3)]^-$ (R = Me, Ph) Containing the Terminal Alkoxide Ligand: Relevance to the Nickel Site of Oxidized-Form [NiFe] Hydrogenases. *Inorg. Chem.* **2008**, *47*, 7908-7913.

(13) Hanss, J.; Krüger, H. J. First Isolation and Structural Characterization of a Nickel(III) Complex Containing Aliphatic Thiolate Donors. *Angew. Chem. Int. Ed.* **1998**, *37*, 360-363.

(14) (a) Blake, A. J.; Gould, R. O.; Halcrow, M. A.; Holder, A. J.; Hyde, T. I.; Schröder, M. Nickel thioether chemistry: a re-examination of the electrochemistry of $[Ni([9]aneS_3)_2]^{2+}$. The single-crystal X-ray structure of a nickel(III) thioether complex, $[Ni^{III}([9]aneS_3)_2][H_5O_2]_3[ClO_4]_6$([9]aneS$_3$= 1,4,7-trithiacyclononane). *J. Chem. Soc. Dalton Trans.* **1992**, 3427-3431. (b) Stephen, E.; Huang, D.; Shaw, J. L.; Blake, A. J.; Collison, D.; Davies, E. S.; Edge, R.; Howard, J. A. K.; McInnes, E. J. L.; Wilson, C.; Wolowska, J.; McMaster, J.; Schröder, M. Redox Non-Innocence of Thioether Crowns: Spectroelectrochemistry and Electronic Structure of Formal Nickel(III) Complexes of Aza–Thioether Macrocycles. *Chem. Eur. J.* **2011**, *17*, 10246-10258.

(15) Sellmann, D.; Binder, H.; Häußinger, D.; Heinemann, F. W.; Sutter, J. Transition metal complexes with sulfur ligands: Part CXLIV. Square planar nickel complexes with NiS_4 cores in three different oxidation states: synthesis, X-ray structural and spectroscopic studies. *Inorg. Chim. Acta.* **2000**, *300*, 829-836.

(16) Glaser, T.; Kesting, F.; Beissel, T.; Bill, E.; Weyhermüller, T.; Meyer-Klaucke, W.; Wieghardt, K. Spin-Dependent Delocalization in Three Isostructural Complexes $[LFeNiFeL]^{2+/3+/4+}$ (L = 1,4,7-(4-tert-Butyl-2-mercaptobenzyl)-1,4,7-triazacyclononane). *Inorg. Chem.* **1999**, *38*, 722-732.

(17) Beissel T.; Birkelbach, F.; Bill, E.; Glaser, Y.; Kesting, F.; Krebs, C.; Weyhermüller, T.; Wieghardt, K.; Butzlaff, C.; Trautwein, A. X. Exchange and Double-Exchange Phenomena in

Linear Homo- and Heterotrinuclear Nickel(II,III,IV) Complexes Containing Six μ_2-Phenolato or μ_2-Thiophenolato Bridging Ligands. *J. Am. Chem. Soc.* **1996**, *118*, 12376-12390.

(18) (a) Lubitz, W.; Ogata, H.; Rüdiger, O.; Reijerse, E. Hydrogenases. *Chem. Rev.* **2014**, *114*, 4081−4148. (b) Can, M.; Armstrong, F. A.; Ragsdale, S. W. Structure, Function, and Mechanism of the Nickel Metalloenzymes, CO Dehydrogenase, and Acetyl-CoA Synthase. *Chem. Rev.* **2014**, *114*, 4149-4174.

(19) Tang, F.; Rath, N. P.; Mirica, L. M. Stable bis(trifluoromethyl)nickel(III) complexes. *Chem. Commun.* **2015**, *51*, 3113-3116.

(20) Wieghardt, K.; Walz, W.; Nuber, B.; Weiss, J.; Ozarowski, A.; Stratemeier, H.; Reinen, D. Crystal structure of bis[bis(1,4,7-triazacyclononane)nickel(III)] dithionate heptahydrate and its single-crystal EPR spectrum. *Inorg. Chem.* **1986**, *25*, 1650-1654.

(21) Gore, E. S.; Busch, D. H. Stable octahedral, low-spin nickel(III) complexes of a tetradentate macrocyclic ligand having saturated nitrogen donors. *Inorg. Chem.* **1973**, *12*, 1-3.

(22) Bhowmick, I.; Roehl, A. J.; Neilson, J. R.; Rappé, A. K.; Shores, M. P. Slow magnetic relaxation in octahedral low-spin Ni(III) complexes. *Chem. Sci.* **2018**, *9*, 6564-6571.

(23) Konno, T. Aggregation of Octahedral Thiolato Complexes by Forming Sulfur-Bridged Structures with Transition Metal Ions. *Bull. Chem. Soc. Jpn.* **2004**, *77*, 627-649.

(24) Yoshinari, N.; Konno, T. Chiral Phenomena in Multinuclear and Metallosupramolecular Coordination Systems Derived from Metalloligands with Thiol-Containing Amino Acids. *Bull. Chem. Soc. Jpn.* **2018**, *91*, 790-812.

(25) Kouno, M.; Yoshinari, N.; Kuwamura, N.; Yamagami, K.; Sekiyama, A.; Okumura, M.; Konno, T. Valence Interconversion of Octahedral Nickel(II/III/IV) Centers. *Angew. Chem. Int. Ed.* **2017**, *56*, 13762-13766.

(26) Amir, N.; Motonishi, M.; Fujita, M.; Miyashita, Y.; Fujisawa, K.; Okamoto, K. Synthesis of Novel S-Bridged Heterotrinuclear Complexes Containing Six-Membered Chelate Rings: Structural, Spectroscopic, and Electrochemical Properties of $[Co\{Rh(apt)_3\}_2]^{3+}$ (apt = 3-Aminopropanethiolate). *Eur. J. Inorg. Chem.* **2006**, 1041-1049.

(27) Kouno, M.; Kuwamura, N.; Yoshinari, N.; Konno, T. 3-Aminopropanethiol versus 2-Aminoethanethiol Leading to Different S-bridged Multinuclear Structures Composed of Rhodium(III) Octahedrons. *Chem. Lett.* **2017**, *46*, 1542-1545.

(28) Kouno, M.; Minami, K.; Kuwamura, N.; Konno, T. A Mixed-valence Copper(I)-Copper(II) Core Supported by Rhodium(III) Octahedrons with 3-Aminopropanethiolate. *Chem. Lett.* **2019**, *48*, 122-125.

(29) Kouno, M.; Kuwamura, N.; Konno, T. Interconversion between square-planar palladium(II) and octahedral palladium(IV) centres in a sulfur-bridged trinuclear structure. *Chem. Commun.* **2021**, *57*, 1336-1339.

(30) Falvello, L. R. Jahn–Teller effects in solid-state co-ordination chemistry. *J. Chem. Soc. Dalton Trans.* **1997**, 4463-4475.

(31) Halcrow, M. A. Jahn–Teller distortions in transition metal compounds, and their importance in functional molecular and inorganic materials. *Chem. Soc. Rev.* **2013**, *42*, 1784-1795.

(32) Konno, T.; Nakamura, K.; Okamoto, K.; Hidaka, J. Preparation and Some Properties of Linear-Type S-Bridged $Ir^{III}Co^{III}Ir^{III}$ Trinuclear Complexes with 2-Aminoethanethiolate (aet) or L-Cysteinate (L-cys). Crystal Structure of ΔΛ-$[Co\{Ir(aet)_3\}_2](NO_3)_3$. *Bull. Chem. Soc. Jpn.* **1993**, *66*, 2582-2589.

(33) Dunitz, J. D.; Schomaker, V.; Trueblood, K. N. Interpretation of atomic displacement parameters from diffraction studies of crystals. *J. Phys. Chem.* **1988**, *92*, 856-867.

(34) Fedin, M. V.; Veber, S. L.; Bagryanskaya, E. G.; Ovcharenko, V. I. Electron paramagnetic resonance of switchable copper-nitroxide-based molecular magnets: An indispensable tool for intriguing systems. *Coord. Chem. Rev.* **2015**, *289–290*, 341-356.

(35) (a) Hitchman, M. A.; Maaskant, W.; van der Plas, J.; Simmons, C. J.; Stratemeier, H. Cooperative Jahn−Teller Interactions in Dynamic Copper(II) Complexes. Temperature Dependence of the Crystal Structure and EPR Spectrum of Deuterated Ammonium Copper(II) Sulfate Hexahydrate. *J. Am. Chem. Soc.* **1999**, *121,* 1488-1501. (b) Prescimone, A.; Morien, C.; Allan, D.; Schlueter, J. A.; Tozer, S. W.; Manson, J. L.; Parsons, S.; Brechin, E. K.; Hill, S. Pressure-Driven Orbital Reorientations and Coordination-Sphere Reconstructions in $[CuF_2(H_2O)_2(pyz)]$. *Angew. Chem. Int. Ed.* **2012**, *51*, 7490-7494. (c) McMonagle, C. J.; Comar, P.; Nichol, G. S.; Allan, D. R.; González, J.; Barreda-Argüeso, J. A.; Rodríguez, F.; Valiente, R.; Turner, G. F.; Brechin, E. K.; Moggach, S. A. Pressure-and temperature induced phase transitions, piezochromism, NLC behaviour and pressure controlled Jahn–Teller switching in a Cu-based framework. *Chem. Sci.* **2020**, *11*, 8793–8799. (d) Scatena, R.; Andrzejewski, M.; Johnson, R. D.; Macchi, P. Pressure-induced Jahn–Teller switch in the homoleptic hybrid perovskite

[$(CH_3)_2NH_2$]Cu(HCOO)$_3$: orbital reordering by unconventional degrees of freedom. *J. Mater. Chem. C* **2021**, *9*, 8051–8056.

(36) (a) Prout, K.; Edwards, A.; Mtetwa, V.; Murray, J.; Saunders, J. F.; Rossotti, F. J. C. Structure and Stability of Carboxylate Complexes. 20. Diaqua Bis(methoxyacetato) Complexes of Nickel(II), Copper(II), and Zinc(II): A Structural Study of the Dynamic Pseudo-Jahn−Teller Effect. *Inorg. Chem.* **1997**, *36,* 2820-2825. (b) Leech, M. A.; Howard, J. A. K.; Dahaoui, S.; Solanki, N. K.; Halcrow, M. A. A solid-state phase transition at 41 K involving the cooperative ordering of a fluxional pseudo-Jahn–Teller Cu^{II} system. *Chem. Commun.* **1999**, 2245–2246. (c) Kilner, C. A.; Halcrow, M. A. An unusual discontinuity in the thermal spin transition in [Co(terpy)$_2$][BF_4]$_2$. *Dalton Trans.* **2010**, *39*, 9008–9012.

(37) Sheldrick, G. M. A short history of SHELX. *Acta Cryst.* **2008**, *A64*, 112-113.

(38) Spek, A. L. Structure Validation in Chemical Crystallography. *Acta Cryst.* **2009**, *D65*, 148-155.

(39) Frisch, M. J.; Trucks, G. W.; Schlegel, H. B.; Scuseria, G. E.; Robb, M. A.; Cheeseman, J. R.; Scalmani, G.; Barone, V.; Mennucci, B.; Petersson, G. A.; Nakatsuji, H.; Caricato, M.; Li, X.; Hratchian, H. P.; Izmaylov, A. F.; Bloino, J.; Zheng, G.; Sonnenberg, J. L.; Hada, M.; Ehara, M.; Toyota, K.; Fukuda, R.; Hasegawa, J.; Ishida, M.; Nakajima, T.; Honda, Y.; Kitao, O.; Nakai, H.; Vreven, T.; Montgomery, Jr., J. A.; Peralta, J. E.; Ogliaro, F.; Bearpark, M.; Heyd, J. J.; Brothers, E.; Kudin. K. N.; Staroverov, V. N.; Kobayashi, E.; Normand, J.; Raghavachari, K.; Rendell, A.; Burant, J. C.; Iyengar, S. S.; Tomasi, J.; Cossi, M.; Rega, N.; Millam, J. M.; Klene, M.; Knox, J. E.; Cross, J. B.; Bakken, V.; Adamo, C.; Jaramillo, J.; Gomperts, R.; Stratmann, R. E.; Yazyev, O.; Austin, A.; Cammi, R.; Pomelli, C.; Ochterski, J. W.; Martin, R. L.; Morokuma, K.;

Zakrzewski, V. G.; Voth, G. A.; Salvador, P.; Dannenberg, J. J.; Dapprich, S.; Daniels, A. D.; Farkas, O.; Foresman, J. B.; Ortiz, J. V.; Cioslowski, J.; Fox, D. J. Gaussian, Inc., Wallingford CT, 2009.

(40) Nakanishi, K.; Yagi, S.; Ohta, T. XAFS Measurements under Atmospheric Pressure in the Soft X-ray Region. *AIP Conf. Proc.* **2010**, *1234*, 931-934.

(41) Yamagami, K.; Fujiwara, H.; Imada, S.; Kadono, T.; Yamanaka, K.; Muro, T.; Tanaka, A.; Itai, T.; Yoshinari, N.; Konno, T.; Sekiyama, A. Local 3d Electronic Structures of Co-Based Complexes with Medicinal Molecules Probed by Soft X-ray Absorption. *J. Phys. Soc. Jpn.* **2017**, *84*, 074801.